The final version is published in Journal of Surveying Engineering (2018) 144(2):04018003, and is available under https://ascelibrary.org/doi/10.1061/%28ASCE%29SU.1943-5428.0000252

Satellite clock modelling in single-frequency PPP-RTK processing

Kan Wang [1], Amir Khodabandeh [2], Peter J.G. Teunissen [3] and Nandakumaran Nadarajah [4]

ABSTRACT

The real-time kinematic precise point positioning (PPP-RTK) technique enables integer ambiguity resolution by providing single-receiver users with information on the satellite phase biases next to the standard precise point positioning (PPP) corrections. Using undifferenced and uncombined observations, rank deficiencies existing in the design matrix need to be eliminated to form estimable parameters. In this contribution, the estimability of the parameters are studied in single-frequency ionosphere-weighted scenario, given a dynamic satellite clock model in the network Kalman filter. In case of latency of the network corrections, the estimable satellite clocks, satellite phase biases and ionospheric delays need to be predicted over short time spans. With and without satellite clock models incorporated in the network Kalman filter, different approaches are used to predict the network corrections. In this contribution, we show how the predicted network corrections response to the presence and absence of satellite clock models. These differences in the predicted network corrections are also reflected in the user positioning results. Using three different 1 Hz global positioning system (GPS) single-frequency data sets, two user stations in one small-scale network are used to compute the positioning results applying predicted network corrections. The latency of the network products ranges from 3 to 10 s. We observe that applying strong satellite clock constraints in the network Kalman filter, i.e., with the process noise of 1 or 0.5 mm per

[1]Research Associate, GNSS Research Centre, Curtin University, GPO Box U1987, Perth, WA 6845, Australia (corresponding author). E-mail: kan.wang@curtin.edu.au

[2]Research Fellow, GNSS Research Centre, Curtin University, GPO Box U1987, Perth, WA 6845, Australia.

[3]Professor, GNSS Research Centre, Curtin University, GPO Box U1987, Perth, WA 6845, Australia; Department of Geoscience and Remote Sensing, Delft University of Technology, PO Box 5048, 2600 GA Delft, The Netherlands.

[4]Research Fellow, GNSS Research Centre, Curtin University, GPO Box U1987, Perth, WA 6845, Australia.

square root of second, reduces the root mean squares (RMS) of the user positioning results within centimetres to decimetres for latencies larger than 6 s, compared to the cases without satellite clock model.

Keywords: Single-frequency, PPP-RTK, Satellite clock modelling, Prediction.

INTRODUCTION

Using external information on satellite orbits and satellite clocks provided by, e.g., the International Global Navigation Satellite System (GNSS) Service (IGS, Dow et al. 2009), the kinematic precise point positioning (PPP) results can nowadays reach cm-level accuracy (Yu and Gao 2017). However, to reach such an accuracy, long convergence time from tens of minutes to hours can be required (Banville et al. 2014, Leandro et al. 2011, Yu and Gao 2017). For single-frequency users, the precision of the kinematic PPP results by applying also external ionospheric information is normally at dm-level (Huisman et al. 2012, van Bree and Tiberius 2012).

In network real-time kinematic (RTK) positioning, corrections are provided to the user in the 'observation-domain'. One can equivalently convey the information content in the network observations through physical parameters e.g. satellite clocks, instrumental delays and atmospheric biases. By employing such 'parameter-space' presentation, real-time kinematic precise point positioning (PPP-RTK) provides parameter corrections that have a lower sending-rate, thus consuming a lower bandwidth for transmitting the corrections to the user (Wübbena et al. 2005). The PPP-RTK technique enables single-receiver integer ambiguity resolution (IAR) by providing users the satellite phase biases apart from the satellite orbits and the satellite clocks. In addition to that, the ionospheric delays, which are spatially interpolated for the user, can also be provided to speed up IAR (Odijk et al. 2014b). During the last ten years, diverse studies have been performed to enable fast integer ambiguity resolution and thus realise high-precision user positioning results in short time spans using dual-frequency and combined global positioning system (GPS) observations (Collins 2008, Ge et al. 2008, Geng et al. 2011, Laurichesse and Mercier 2007, Loyer

et al. 2012, Teunissen et al. 2010). For a detailed review, see Teunissen and Khodabandeh (2015). For single-frequency PPP-RTK users, cm-level accuracy can also be reached for real-time kinematic positioning within several minutes using undifferenced and uncombined observations, even with low-cost GNSS receivers (Odijk et al. 2012b). It was shown that single-frequency GPS + BeiDou navigation satellite system (BDS) RTK positioning with low-cost receivers can be competitive to dual-frequency GPS-only solutions using survey-grade receivers (Odolinski and Teunissen 2017). Using multi-GNSS signals, Li et al. (2017) proposed a new array-aided state-space RTK concept for single-frequency data processing, which improves the accuracy of the positioning results when increasing the number of the array antennas.

Using undifferenced and uncombined GPS L1 observations in PPP-RTK network processing, with the help of the *S*-system theory (Baarda 1981, Teunissen 1985), rank deficiencies of the design matrix are removed, leading to estimable combinations of the parameters (Odijk et al. 2012b). The estimable satellite clocks, satellite phase biases and the interpolated user-specific ionospheric delays can then be provided to the user (Odijk et al. 2012b, Odijk et al. 2014b). Due to the latencies of the PPP-RTK network products, the network corrections have to be predicted to bridge the time gap between the estimation of the network corrections and the user positioning. According to the study of Laurichesse et al. (2010), the overall latency of the network products based on a real-time integer PPP demonstrator developed by CNES is between 6 to 8 s. Leandro et al. (2011) have also reported a total correction latency for the Real Time Extended (RTX) system (via a satellite link) of smaller than 5.6 s in 99% of the cases. To bridge the latency of the network products, a dynamic satellite clock model can be incorporated into the network Kalman filter under single-frequency scenario with the ionospheric delays spatially constrained between stations in a small-scale network (ionosphere-weighted model (Odijk 2002)). In Li et al. (2017), the estimability of the parameters without the satellite clock model are studied for single-frequency scenario based on the assumption that the atmospheric delays are the same for all stations. In this

contribution, with the help of S-system theory, we study the estimability of the parameters applying the satellite clock model using undifferenced and uncombined observations under single-frequency ionosphere-weighted scenario.

Using 1 Hz GPS single-frequency data from a small-scale network, estimated and predicted network corrections are studied and discussed without and with clock constraints of different strengths. The influences of the satellite clock models on the predicted network corrections lead to changes in the user positioning results. Using two user stations located within the network, based on the data of three different hours within one day, different sets of predicted network corrections are applied by the users. Without satellite clock constraints, the satellite clock estimates are predicted with the help of post-computed satellite clock rates, which can either be obtained by fitting polynomials using the satellite clock estimates, or by directly setting to a constant value. With the satellite clock model incorporated in the network Kalman filter, the satellite clock rates are estimated in the Kalman filter and are used to predict the satellite clocks for different latencies. In this contribution, the influences of the predicted network corrections (with and without applying satellite clock models) on the user positioning results are analysed and discussed with a latency ranging from 3 to 10 s using GPS L1 observations.

In section "Processing Strategy", we firstly study the estimability of the network parameters without and with the satellite clock models under single-frequency and ionosphere-weighted scenario. A single-frequency network full-rank model applicable to an arbitrary GNSS is developed with dynamic satellite clock model incorporated into the network Kalman filter. The data selection and the impacts of the satellite clock models on the estimated and the predicted network parameters are then discussed in the subsequent section. In section "Latency and user positioning results", the influences of the satellite clock modelling on the user positioning results are analysed and discussed for a latency ranging from 3 to 10 s. Section "Conclusion" concludes this contribution.

PROCESSING STRATEGY

For the single-frequency scenario, the Observed-minus-Computed (O-C) terms of the phase ($\Delta\phi^s_{r,j}$) and the code observations ($\Delta p^s_{r,j}$) can be formulated as (Hofmann-Wellenhof et al. 2008, Teunissen and Montenbruck 2017):

$$E(\Delta\phi^s_{r,j}) = g^s_r\tau_r + dt_r - dt^s - \mu_j\iota^s_r + \delta_{r,j} - \delta^s_{,j} + \lambda_j z^s_{r,j}, \quad (1)$$

$$E(\Delta p^s_{r,j}) = g^s_r\tau_r + dt_r - dt^s + \mu_j\iota^s_r + d_{r,j} - d^s_{,j}, \quad (2)$$

where the subindices r, j and the superindex s denote the receiver r ($r = 1, \cdots, n$), frequency f_j and satellite s ($s = 1, \cdots, m$), respectively. τ_r represents the zenith tropospheric delay (ZTD) for receiver r (after removing a priori values) with its mapping function g^s_r for receiver r and satellite s in front of it. In this study, the hydrostatic components of the ZTDs, i.e., the a priori ZTDs, are modeled with the Saastamoinen model (Saastamoinen 1972) and are included in the O-C terms. The wet components of the ZTDs are estimated. dt_r and dt^s represent the receiver and the satellite clock, respectively, and ι^s_r stands for the ionospheric delay for receiver r and satellite s on a reference frequency f_1 with coefficient $\mu_j = \frac{f_1^2}{f_j^2}$. The receiver and satellite hardware delays are denoted by $\delta_{r,j}$ and $\delta^s_{,j}$ for phase observations, and $d_{r,j}$ and $d^s_{,j}$ for code observations, respectively. The integer-valued ambiguity $z^s_{r,j}$ is multiplied with the wavelength λ_j. $E(.)$ denotes expectation operator.

Since the processing in this study is based on GPS L1 observations from a small-scaled network (with inter-station distances within 50 km), weighted constraints are applied on the between-station ionospheric delays (Odijk 2002):

$$d\iota^s_{r\neq 1} = \iota^s_{r\neq 1} - \iota^s_1, \quad (3)$$

where $d\iota^s_r$ ($r = 2, \cdots, n$) represents pseudo-observations having zero sample values with distance-dependent weights. The larger the between-station distances, the smaller the weights become.

Using undifferenced and uncombined single-frequency GPS observations, as shown in

Eqs. (1) and (2), singularities exist between the parameters. Based on the S-system theory (Baarda 1981, Teunissen 1985), we form the estimable parameters by constraining a minimum set of S-basis parameters, so that the full-rank property of the design matrix can be recovered (Teunissen et al. 2010). The O-C terms of the phase and the code observations can be reformulated as:

$$E(\Delta\phi^s_{r,j}) = g^s_r\tilde{\tau}_r + d\tilde{t}_r - d\tilde{t}^s - \mu_j\tilde{\imath}^s_r + \tilde{\delta}_{r,j} - \tilde{\delta}^s_{,j} + \lambda_j\tilde{z}^s_{r,j}, \quad (4)$$

$$E(\Delta p^s_{r,j}) = g^s_r\tilde{\tau}_r + d\tilde{t}_r - d\tilde{t}^s + \mu_j\tilde{\imath}^s_r + \tilde{d}_{r,j} - \tilde{d}^s_{,j}, \quad (5)$$

where the estimable parameters $\tilde{\tau}_r$, $d\tilde{t}_r$, $d\tilde{t}^s$, $\tilde{\imath}^s_r$, $\tilde{\delta}_{r,j}$, $\tilde{\delta}^s_{,j}$, $\tilde{d}_{r,j}$, $\tilde{d}^s_{,j}$ and $\tilde{z}^s_{r,j}$ are listed in Table 1. From Table 1 we see that the ZTDs are estimated relatively based on the assumption that the ZTD mapping functions between stations in a small-scaled network are similar to each other ($g^s_{r\neq 1} \approx g^s_1$).

The estimable parameters (see Table 1) are estimated in a Kalman filter in the Curtin PPP-RTK network software (Odijk et al. 2017). The ionospheric delays, the receiver and satellite hardware biases and the ZTDs are linked in time with a random-walk process. The vector of the time-updated parameters $\hat{x}_{i|i-1}$ and the corresponding variance-covariance matrix $Q_{i|i-1}$ at epoch i are calculated based on the estimation of the last epoch, i.e., epoch $i-1$:

$$\hat{x}_{i|i-1} = \Phi_{i|i-1}\hat{x}_{i-1|i-1}, \qquad Q_{i|i-1} = \Phi_{i|i-1}Q_{i-1|i-1}\Phi^T_{i|i-1} + S_{x_i}, \quad (6)$$

where $\hat{x}_{i-1|i-1}$ and $Q_{i-1|i-1}$ represent the filtered parameters and the corresponding variance-covariance matrix at epoch $i-1$, respectively. The transition matrix $\Phi_{i|i-1}$ time-predicts $\hat{x}_{i|i-1}$ from epoch $i-1$. S_{x_i} represents the variance-covariance matrix of the system noise at the epoch i.

Instead of estimating the satellite clock parameters as time-unlinked parameters as shown in Table 1, dynamic models can be applied to constrain the temporal behaviours of the satellite clocks. As described in Wang et al. (2017), the satellite clock parameters can be

modelled with the help of the satellite clock rate $\dot{dt}^s$:

$$\begin{bmatrix} dt^s(t_i) \\ \dot{dt}^s(t_i) \end{bmatrix} = \Phi^s_{i|i-1} \begin{bmatrix} dt^s(t_{i-1}) \\ \dot{dt}^s(t_{i-1}) \end{bmatrix} + \begin{bmatrix} \epsilon^s(t_i) \\ \dot{\epsilon}^s(t_i) \end{bmatrix}, \tag{7}$$

with

$$\Phi^s_{i|i-1} = \begin{bmatrix} 1 & \Delta t_i \\ 0 & 1 \end{bmatrix}, \qquad \Delta t_i = t_i - t_{i-1}, \tag{8}$$

where ϵ^s and $\dot{\epsilon}^s$ denote the system noise of the satellite clock and the satellite clock rate for satellite s, respectively.

Based on the study of Senior et al. (2008), different generations and types of the GPS satellite clocks may show different noise behaviours for different averaging time. In order not to increase the complexity and computational load for real-time usage (Hauschild and Montenbruck 2009), in this study, we do not attempt to distinguish the noise types between different GPS satellite clocks. The white frequency noise (WFN) is assumed to be the dominant noise type (Wang et al. 2017), and the 2-state (clock and clock rate) variance matrix for WFN in the Kalman filter, i.e., the variance matrix for the terms ϵ^s and $\dot{\epsilon}^s$ in Eq. (7), is formulated as (van Dierendonck et al. 1984):

$$S_{dt^s}(t_i) = \begin{bmatrix} \frac{h_0}{2}\Delta t_i & 0 \\ 0 & \frac{h_0}{2\Delta t_i} \end{bmatrix} \cdot c^2 = q^2_{dt^s} \begin{bmatrix} \frac{\Delta t_i}{2} & 0 \\ 0 & \frac{1}{2\Delta t_i} \end{bmatrix} \tag{9}$$

with

$$h_0 = \sigma_A^2 \cdot 2\tau, \qquad q_{dt^s} = \sqrt{h_0} \cdot c, \tag{10}$$

where c denotes the speed of light. σ_A and τ represent the Allan deviation (Allan 1987) and the corresponding averaging time, respectively. For WFN, with a slope of -0.5 in the Sigma-Tau-Diagram of the Allan deviations (Riley 2008), the parameter q_{dt^s} is a constant value.

Applying the satellite clock model (see Eq. (7)), the estimability of the receiver and satellite clocks changes, and the ZTDs are able to be estimated absolutely for each station. The changes in the estimable parameters (compared to those listed in Table 1) are listed in Table 2. Compared to the case with unlinked satellite clocks (see Table 1), the reference receiver clocks at the third epoch (and beyond), i.e., $dt_1(t_{i>2})$, are not constrained as S-basis parameters anymore.

Based on Tables 1 and 2, the number of the observation equations (including the constraint equations, denoted as l_o), the number of the estimable parameters (l_u) and the number of the redundancies (l_r) are shown in Fig. 1 for the cases without satellite clock model. The addition of the numbers after applying the satellite clock model is marked with blue. Based on Eqs. (4) and (5), $2nm$ phase and code measurements are received by the receivers. In addition to that, the ionosphere-weighted model (see Eq. (3)) provides $(n-1)m$ constraint equations. From the second epoch t_2 (without satellite clock model), with the time-links of the ZTDs (n), the receiver hardware biases ($2n$), the satellite hardware biases ($2m$), the ionospheric delays (nm) and the ambiguities ($(n-1)(m-1)$), $2mn+m+2n+1$ additional time-constraint equations are available. Having satellite clock model, m more constraint equations are available for $t_{i>2}$ for the satellite clocks and the satellite clock rates, respectively. This leads to an addition of l_o of $2m$. Based on Table 1, without satellite clock model, $2nm+2n-2$ and $2nm+3n+2m$ estimable parameters need to be estimated at the first epoch and for $t_{i>1}$, respectively. Applying satellite clock model makes the estimation of the absolute ZTDs possible (see Table 2). This leads to one more estimable parameter at t_1. For $t_{i>2}$, m estimable satellite clock rates and the estimable reference receiver clock are also added to l_u. This leads to an addition of $m+1$ for l_u in total for $t_{i>2}$. As a result, from the box for l_r in Fig. 1 we see that the redundancy at t_1 has decreased by 1 applying satellite clock model due to the change from relative to absolute ZTD estimation (with an additional parameter). However, for $t_{i>2}$, the redundancy l_r has increased by $m-1$ after applying satellite clock model.

With Table 2 and Eq. (7), we can obtain:

$$
\begin{aligned}
d\tilde{\tilde{t}}^s(t_i) &= dt^s(t_i) + d^s_{,j}(t_1) - (dt_1(t_1) + d_{1,j}(t_1)) - \mu_j \iota^s_1(t_1) - \frac{t_i - t_1}{\Delta t_2}(dt_1(t_2) \qquad (11)\\
&\quad -dt_1(t_1))\\
&= dt^s(t_{i-1}) + \Delta t_i \dot{dt}^s(t_{i-1}) + \epsilon^s(t_i) + d^s_{,j}(t_1) - (dt_1(t_1) + d_{1,j}(t_1)) - \mu_j \iota^s_1(t_1)\\
&\quad -(\frac{t_{i-1} - t_1}{\Delta t_2} + \frac{\Delta t_i}{\Delta t_2})(dt_1(t_2) - dt_1(t_1))\\
&= d\tilde{\tilde{t}}^s(t_{i-1}) + \Delta t_i \dot{d\tilde{\tilde{t}}}^s(t_{i-1}) + \epsilon^s(t_i),\\
\dot{d\tilde{\tilde{t}}}^s(t_i) &= \dot{dt}^s(t_i) - \frac{1}{\Delta t_2}(dt_1(t_2) - dt_1(t_1)), \qquad (12)\\
&= \dot{dt}^s(t_{i-1}) + \dot{\epsilon}^s(t_i) - \frac{1}{\Delta t_2}(dt_1(t_2) - dt_1(t_1)),\\
&= \dot{d\tilde{\tilde{t}}}^s(t_{i-1}) + \dot{\epsilon}^s(t_i).
\end{aligned}
$$

From Eqs. (11) and (12) we see that the satellite clock model (see Eq. (7)) also applies for the new *estimable* satellite clocks $d\tilde{\tilde{t}}^s$ and satellite clock rates $\dot{d\tilde{\tilde{t}}}^s$:

$$
\begin{bmatrix} d\tilde{\tilde{t}}^s(t_i) \\ \dot{d\tilde{\tilde{t}}}^s(t_i) \end{bmatrix} = \Phi^s_{i|i-1} \begin{bmatrix} d\tilde{\tilde{t}}^s(t_{i-1}) \\ \dot{d\tilde{\tilde{t}}}^s(t_{i-1}) \end{bmatrix} + \begin{bmatrix} \epsilon^s(t_i) \\ \dot{\epsilon}^s(t_i) \end{bmatrix}, \qquad (13)
$$

With the estimable satellite clocks $d\tilde{t}^s$ (without clock model), satellite phase biases $\tilde{\delta}^s_{,j}$ and the network-derived user ionospheric delays $\tilde{\iota}^s_u$ (Wang et al. 2017) provided to the users, the O-C terms of the phase and the code observations at the user side can be formulated as follows:

$$
\begin{aligned}
E(\Delta\phi^s_{u,j}) + d\tilde{t}^s + \tilde{\delta}^s_{,j} + \mu_j \tilde{\iota}^s_u &= \Delta\tilde{\rho}^s_u + d\tilde{t}_u + \tilde{\delta}_{u,j} + \lambda_j \tilde{z}^s_{u,j}, \qquad (14)\\
E(\Delta p^s_{u,j}) + d\tilde{t}^s - \mu_j \tilde{\iota}^s_u &= \Delta\tilde{\rho}^s_u + d\tilde{t}_u + \tilde{d}_{u,j} - \tilde{d}^s_{,j}, \qquad (15)
\end{aligned}
$$

where the term $\Delta\tilde{\rho}^s_u$ contains the increment of the user station coordinates and the *relative* user ZTD (see Table 1) in the slant direction. If the satellite clock models are applied, the

estimable satellite clocks $d\tilde{t}^s$ in Eqs. (14) and (15) are replaced by those applying the satellite clock model ($d\tilde{\tilde{t}}^s$) instead:

$$E(\Delta\phi^s_{u,j}) + d\tilde{\tilde{t}}^s + \tilde{\delta}^s_{,j} + \mu_j \tilde{\imath}^s_u = \Delta\tilde{\tilde{\rho}}^s_u + d\tilde{\tilde{t}}_u + \tilde{\delta}_{u,j} + \lambda_j \tilde{z}^s_{u,j}, \quad (16)$$

$$E(\Delta p^s_{u,j}) + d\tilde{\tilde{t}}^s - \mu_j \tilde{\imath}^s_u = \Delta\tilde{\tilde{\rho}}^s_u + d\tilde{\tilde{t}}_u + \tilde{d}_{u,j} - \tilde{d}^s_{,j}, \quad (17)$$

where the term $\Delta\tilde{\tilde{\rho}}^s_u$ contains the increment of the user station coordinate and the *absolute* user ZTD (see Table 2) in the slant direction. $d\tilde{\tilde{t}}_u$ represents the estimable user receiver clock with the form in Table 2.

For the network and the user processing, the a priori standard deviations at the zenith direction are set to be 3 mm (σ_ϕ) and 3 dm (σ_p) for the phase and the code observations, respectively. Given these a priori standard deviations, elevation-dependent weighting function (Eueler and Goad 1991) can be applied to the observations with (Dach et al. 2007):

$$w_\phi(e) = \frac{\sin^2(e)}{\sigma^2_\phi}, \quad (18)$$

$$w_p(e) = \frac{\sin^2(e)}{\sigma^2_p}, \quad (19)$$

where e represents the elevation angle of the observation, and $w_\phi(e)$ and $w_p(e)$ represent the elevation-dependent weights of the phase and the code observations, respectively. During the network processing, the ultra rapid satellite orbits provided by the IGS with predicted satellite positions (Dow et al. 2009, Springer and Hugentobler 2001) and the precise station coordinates provided by the Geoscience Australia (GA, Geoscience Australia 2017) are used for generating the O-C terms and are not estimated. As shown in Table 3, the ZTDs, the hardware biases and the ionospheric delays are linked in time. The ambiguities are assumed to be constant, and the satellite clocks are estimated for both cases as unlinked and linked parameters. The spatial ionosphere-weighted model is applied with the standard deviation of the between-station single-differenced ionospheric delays set as 0.03 m per 20 km. The

partial integer ambiguity resolution (Odijk et al. 2014a) with a pre-defined ambiguity success rate of 99.99% is used in both the network and the user processing.

NETWORK CORRECTIONS WITHOUT AND WITH SATELLITE CLOCK MODELLING

In the processing, we used 1 Hz GPS L1 data from a small-scale network located in Victoria, Australia (see Fig. 2) on March 28, 2017 from 5:00 to 7:00, from 13:00 to 15:00 and from 21:00 to 23:00 in GPS Time (GPST). The network consists of 4 stations (see the yellow marks in Fig. 2) with an inter-station distance ranging from 19.6 to 42.9 km. Two stations are used as the user stations (see the red marks in Fig. 2). The network stations are all using receivers of the type TRIMBLE NETR9, and the two user stations are using receivers of the types LEICA GRX1200GGPRO and SEPT POLARX4, respectively. Since the network products are assumed to be provided to the users over a long time period, the user processing starts one hour after the network processing. For newly risen satellites during the user processing, the network products of the first 8 minutes are considered within the initialization phase of the network Kalman filter and are not used by the user. The elevation mask is set to be 10 degrees. In this study, the GPS L1 observations are used for the network and the user processing. However, we remark that the estimability of the parameters introduced in the previous section applies also for single-frequency signals of other GNSS or multi-GNSS single-frequency signals. When processing multi-GNSS single-frequency observations, the inter-system biases (ISBs) need to be properly considered (Odijk et al. 2012a).

As shown by Khodabandeh and Teunissen (2015), the between-satellite differences of the network corrections take an active role in user positioning. As a result, for the user positioning, the network products are effective or largely effective at the between-satellite level, if the receiver clocks and hardware biases are unlinked or very weakly linked in time. Based on Tables 1 and 2, the between-satellite clocks without ($d\tilde{t}^{1s}$) and with the satellite

clock models ($d\tilde{\tilde{t}}^{1s}$) have the following formulation:

$$d\tilde{t}^{1s}(t_i) = dt^{1s}(t_i) + d^{1s}_{,j}(t_1) - \mu_j \iota^{1s}_1(t_1) - g^{1s}_1(t_i)\tau_1(t_1), \quad (20)$$

$$d\tilde{\tilde{t}}^{1s}(t_i) = dt^{1s}(t_i) + d^{1s}_{,j}(t_1) - \mu_j \iota^{1s}_1(t_1). \quad (21)$$

The difference between $d\tilde{\tilde{t}}^{1s}$ and $d\tilde{t}^{1s}$ at the time point t_i is thus the term $g^{1s}_1(t_i)\tau_1(t_1)$. $\tau_1(t_1)$ can be obtained by:

$$\tau_1(t_1) = \frac{d\tilde{\tilde{t}}^{1s}(t_i) - d\tilde{t}^{1s}(t_i)}{g^{1s}_1(t_i)}. \quad (22)$$

As examples, Fig. 3(a) shows the between-satellite differences of the ZTD mapping functions g^{1s}_1 for the satellite pairs G07-G09, G07-G30, G07-G23, G07-G27 and the $\tau_1(t_1)$ obtained from Eq. (22) using the between-satellite clock estimates $d\hat{\tilde{t}}^{1s}$ without satellite clock model and $d\hat{\tilde{\tilde{t}}}^{1s}$ with satellite clock model ($q_{dt^s} = 7$ mm/$\sqrt{\text{s}}$) from 14:00 to 15:00 on March 28, 2017. The signals of these satellites are received by all network stations from the start of the network processing and the S-basis parameters $\iota^s_1(t_1)$ and $\tau_1(t_1)$ (see Tables 1 and 2) for these satellites relate to the same reference receiver. The time intervals with g^{1s}_1 near zero (with an absolute value smaller than 0.01) are excluded from Fig. 3(b) for purpose of visualisation. From Fig. 3(b) we see that the variance of $\tau_1(t_1)$ increases with decreasing absolute value of g^{1s}_1. Using the data from the satellite pair G07-G27 with relatively large absolute g^{1s}_1 and small changes in the variance of $\tau_1(t_1)$, the mean value of $\tau_1(t_1)$ amounts to around 6 cm.

Fig. 4 shows the formal standard deviations of the estimable between-satellite clocks without and with clock constraint for the satellites G07 and G09 from 14:00 to 15:00 on March 28, 2017. To test the influences of the satellite clock constraints with different strengths on the results, the values 7, 1, and 0.5 mm/$\sqrt{\text{s}}$ are used for the parameter q_{dt^s} (see Eq. (10)) with decreasing system noise. From Fig. 4 we see that the formal standard deviations of the estimable between-satellite clocks for G07 and G09 from 14:00 to 15:00 amount to several decimetres. Applying satellite clock model helps to reduce the formal standard deviations

by millimetres (up to centimetre), and thus improves the precision of the between-satellite clock estimates.

The between-satellite single-frequency combined network corrections without satellite clock model ($\tilde{\omega}^{1s}_{r,j}$) and with satellite clock model ($\tilde{\tilde{\omega}}^{1s}_{r,j}$) are defined as follows (see also Tables 1 and 2):

$$\begin{aligned} \tilde{\omega}^{1s}_{r,j}(t_i) &= d\tilde{t}^{1s}(t_i) + \tilde{\delta}^{1s}_{,j}(t_i) + \mu_j \tilde{\iota}^{1s}_{r}(t_i) \qquad (23) \\ &= dt^{1s}(t_i) + \delta^{1s}_{,j}(t_i) + \mu_j \iota^{1s}_{r}(t_i) - g^{1s}_{1}(t_i)\tau_1(t_1) - z^{1s}_{1,j}\lambda_j, \\ \tilde{\tilde{\omega}}^{1s}_{r,j}(t_i) &= d\tilde{\tilde{t}}^{1s}(t_i) + \tilde{\delta}^{1s}_{,j}(t_i) + \mu_j \tilde{\iota}^{1s}_{r}(t_i) \qquad (24) \\ &= dt^{1s}(t_i) + \delta^{1s}_{,j}(t_i) + \mu_j \iota^{1s}_{r}(t_i) - z^{1s}_{1,j}\lambda_j. \end{aligned}$$

As an example, Fig. 5(a) shows the formal standard deviations of the between-satellite combined network correction $\hat{\sigma}_{\tilde{\omega}^{1s}_{r,j}}$ (without satellite clock model) and $\hat{\sigma}_{\tilde{\tilde{\omega}}^{1s}_{r,j}}$ (with satellite clock model) between the satellites G07 and G09 for the network station WBEE from 14:00 to 15:00 on March 28, 2017. From Fig. 5(a) we see that the dm-level formal standard deviations visible in Fig. 4 are significantly reduced when combining the network corrections. The differences of the formal standard deviations without and with satellite clock model for G07 and G09 from 14:00 to 15:00 are smaller than sub-millimetre.

The different formal standard deviations of the single and the combined network products are caused by the strong correlation among the between-satellite clocks ($d\tilde{t}^{1s}$ without clock model or $d\tilde{\tilde{t}}^{1s}$ with clock model), the between-satellite ionospheric delays $\tilde{\iota}^{1s}_{r}$ and the between-satellite phase biases $\tilde{\delta}^{1s}_{,j}$. Fig. 5(b) shows, e.g., the correlation coefficients of the between-satellite clocks and the sum of the between-satellite ionospheric delays (for the network station WBEE) and the between-satellite phase biases from 14:00 to 15:00 on March 28, 2017 for the satellite pair G07 and G09, which is formulated as:

$$\tilde{\varphi}^{1s}_{r,j} = \tilde{\delta}^{1s}_{,j} + \mu_j \tilde{\iota}^{1s}_{r}. \qquad (25)$$

From Fig. 5(b) we see that the absolute values of the correlation coefficients between $d\tilde{t}^{1s}$ without satellite clock model (or $d\tilde{\tilde{t}}^{1s}$ with satellite clock model) and $\tilde{\varphi}^{1s}_{r,j}$ are large, which indicate strong correlation among the network corrections. Applying satellite clock models slightly reduce the absolute values of the correlation coefficients. The reduced formal standard deviations of the between-satellite combined network corrections (see Fig. 5(a)) compared to those of the between-satellite clocks (see Fig. 4) can be explained by the high correlations shown in Fig. 5(b) (Khodabandeh and Teunissen 2015). Accordingly, although the precision of each individual between-satellite corrections (satellite clocks, satellite phase biases and ionospheric delays) is driven by the code data, the precision of their combined version is at the phase-level.

According to Bevis et al. (1992) and Younes (2016), the wet component of ZTDs can vary from centimetres (or less) in arid regions to as large as 35 cm in humid regions. With the g_1^{1s} for the satellite pairs G07 and G09 (from 14:00 to 15:00 on March 28, 2017) shown in Fig. 3(a) varying from around -0.07 to 0.06, the term $g_1^{1s}(t_i)\tau_1(t_1)$ for G07 and G09 during this time interval thus generally varies from sub-millimetres to millimetres, and does not exceed 2.5 cm in the extreme cases, i.e., with the wet component of ZTD for the reference receiver at t_1 amounting to 35 cm. Based on the small differences of $\tilde{\omega}^{1s}_{r,j}$ and $\tilde{\tilde{\omega}}^{1s}_{r,j}$ for this satellite pair and test interval per definition (see Eqs. (23) and (24)), the estimates of the between-satellite combined network corrections for station WBEE without satellite clock model ($\hat{\tilde{\omega}}^{1s}_{r,j}$) and with satellite clock model ($\hat{\tilde{\tilde{\omega}}}^{1s}_{r,j}$) are compared. For a better visualisation, the between-satellite clock drift and offset derived from the IGS clock biases (IGS clock 2017) for G07 and G09 from 14:00 to 15:00 on March 28, 2017 are subtracted from the between-satellite combined network corrections to generate the residuals:

$$\Delta\hat{\tilde{\omega}}^{1s}_{r,j}(t_i) = \hat{\tilde{\omega}}^{1s}_{r,j}(t_i) - \hat{p}_1^{1s}\cdot(t_i - t_0) - \hat{p}_0^{1s}, \tag{26}$$

$$\Delta\hat{\tilde{\tilde{\omega}}}^{1s}_{r,j}(t_i) = \hat{\tilde{\tilde{\omega}}}^{1s}_{r,j}(t_i) - \hat{p}_1^{1s}\cdot(t_i - t_0) - \hat{p}_0^{1s}, \tag{27}$$

where the satellite clock rate $\hat{p}_1^s$ and offset $\hat{p}_0^s$ are derived from the IGS satellite clock biases $\hat{dt}_{IGS}^s$ with:

$$\hat{dt}_{IGS}^s(t_i) = p_1^s(t_i - t_0) + p_0^s, \tag{28}$$

where t_0 denotes here 14:00 on March 28, 2017.

Fig. 6(a) shows the residuals of the between-satellite combined network corrections without and with satellite clock model (see Eqs. (26) and (27)) for station WBEE for G07 and G09 from 14:00 to 15:00 on March 28, 2017. We see that the results are almost overwritten by each other (with differences within millimetres). Based on Eqs. (23) and (24), the variation of $\Delta\hat{\tilde{\omega}}_{r,j}^{1s}$ and $\Delta\hat{\tilde{\tilde{\omega}}}_{r,j}^{1s}$ should be related to the stochastic behaviours of the satellite clocks (after removing offset and drift) on between-satellite level, possible cycle slips in $z_{1,j}^{1s}$, the variation of the between-satellite phase biases, the between-satellite ionospheric biases and the term $g_1^{1s}(t_i)\tau_1(t_1)$ (for relative ZTD estimation). After adding the between-satellite O-C term of the phase observations for station WBEE ($\Delta\phi_{r,j}^{1s}$, see Eq. (4)) to its between-satellite combined network corrections from 14:00 to 15:00 on March 28, 2017, the short-term variation in Fig. 6(a) at dm-level is reduced to mm-level (see Fig. 6(b)). The expectation of the remaining parts of $\Delta\phi_{r,j}^{1s} + \hat{\tilde{\omega}}_{r,j}^{1s}$ (without satellite clock model) and $\Delta\phi_{r,j}^{1s} + \hat{\tilde{\tilde{\omega}}}_{r,j}^{1s}$ (with satellite clock model) contain the term of the tropospheric delays ($g_r^{1s}\tilde{\tau}_r$ and $g_r^{1s}\tilde{\tilde{\tau}}_r$) and the ambiguities:

$$E(\Delta\tilde{\phi}_{r,j}^{1s}) = E(\Delta\phi_{r,j}^{1s} + \hat{\tilde{\omega}}_{r,j}^{1s}) = g_r^{1s}\tilde{\tau}_r + \lambda_j\tilde{z}_{r,j}^{1s}, \tag{29}$$

$$E(\Delta\tilde{\tilde{\phi}}_{r,j}^{1s}) = E(\Delta\phi_{r,j}^{1s} + \hat{\tilde{\tilde{\omega}}}_{r,j}^{1s}) = g_r^{1s}\tilde{\tilde{\tau}}_r + \lambda_j\tilde{z}_{r,j}^{1s}. \tag{30}$$

The conclusion therefore reads that applying satellite clock model does not generate significant differences in the between-satellite combined network corrections compared to the case without satellite clock model. However, the situation changes in case of latencies, i.e., when the network corrections need to be *predicted*.

In case of latencies, the network corrections are predicted separately for each parameter

(the estimable satellite clocks, satellite phase biases and user-specific ionospheric delays). In correspondence with the settings in the network Kalman filter, the estimable satellite phase biases and user-specific ionospheric delays at the prediction time point $t_i + t_P$ are set to be equal to those at the last estimation time point t_i with t_P denoting the prediction time:

$$\check{\hat{\delta}}^s_{,j}(t_i + t_P) = \hat{\hat{\delta}}^s_{,j}(t_i), \tag{31}$$

$$\check{i}^s_u(t_i + t_P) = \hat{i}^s_u(t_i), \tag{32}$$

where $\hat{\hat{\delta}}^s_{,j}$ and $\hat{i}^s_u$ represent the estimated satellite phase biases on GPS L1 and the user-specific ionospheric delays for the satellite s, respectively. $\check{\hat{\delta}}^s_{,j}$ and $\check{i}^s_u$ represent the predicted satellite phase biases on GPS L1 and the user-specific ionospheric delays for the satellite s, respectively.

The estimable satellite clock (applying satellite clock model) is predicted with the help of the estimated satellite clock rate $\dot{\hat{\tilde{dt}}}^s$ in the Kalman filter:

$$\check{\hat{\tilde{dt}}}^s(t_i + t_P) = \hat{\hat{\tilde{dt}}}^s(t_i) + \dot{\hat{\tilde{dt}}}^s(t_i) \cdot t_P. \tag{33}$$

Alternatively, in case the satellite clock model is not applied in the network processing, the estimable satellite clock can also be predicted with the help of the post-computed satellite clock rates $\dot{\hat{\tilde{dt}}}^s$:

$$\check{\hat{\tilde{dt}}}^s(t_i + t_P) = \hat{\hat{\tilde{dt}}}^s(t_i) + \dot{\hat{\tilde{dt}}}^s(t_i) \cdot t_P. \tag{34}$$

The post-computed satellite clock rates can be obtained by fitting polynomials using the satellite clock estimates without clock constraint $\hat{\tilde{dt}}^s$. Assuming that the estimable satellite clock $\tilde{dt}^s$ without clock model (see Table 1) behaves similarly to a linear polynomial within short time span, the polynomial can be fitted with:

$$E(\tilde{dt}^s(t_i)) = a^s_0 + a^s_1(t_i - t_o), \tag{35}$$

where a_0^s and a_1^s represent the offset and rate of the estimable clock of satellite s at the time point t_i without applying clock model, respectively. t_o represents the starting time of the polynomial fitting. The estimation is performed for all satellites in each epoch, and the estimated parameter $\hat{a}_1^s$ is used as the satellite clock rate $\dot{\hat{\tilde{t}}}^s$ in Eq. (34). In this study, the starting time of the polynomial fitting t_o is set to be t_i-9 s, which means that the satellite clock estimates (without clock model) of the last 10 s are used for the polynomial fitting. We remark that estimating the satellite clock rates by post-computing polynomials using the satellite clock estimates without clock model violates the assumption that we have made in the network Kalman filter. In contrast to that, the prediction based on $\dot{\hat{\tilde{t}}}^s$ directly follows the dynamic model of the satellite clocks in the network Kalman filter.

The predicted combined corrections without ($\check{\tilde{\omega}}_{u,j}^s$) and with satellite clock models ($\check{\tilde{\tilde{\omega}}}_{u,j}^s$) are defined as:

$$\begin{aligned}
\check{\tilde{\omega}}_{u,j}^s(t_i+t_P) &= d\check{\tilde{t}}^s(t_i+t_P)+\check{\tilde{\delta}}_{,j}^s(t_i+t_P)+\mu_j\check{\tilde{\imath}}_u^s(t_i+t_P), \qquad (36)\\
&= d\hat{\tilde{t}}^s(t_i)+\dot{\hat{\tilde{t}}}^s(t_i)\cdot t_P+\hat{\tilde{\delta}}_{,j}^s(t_i)+\mu_j\hat{\tilde{\imath}}_u^s(t_i),\\
&= \hat{\tilde{\omega}}_{u,j}^s(t_i)+\dot{\hat{\tilde{t}}}^s(t_i)\cdot t_P,\\
\check{\tilde{\tilde{\omega}}}_{u,j}^s(t_i+t_P) &= d\check{\tilde{\tilde{t}}}^s(t_i+t_P)+\check{\tilde{\tilde{\delta}}}_{,j}^s(t_i+t_P)+\mu_j\check{\tilde{\tilde{\imath}}}_u^s(t_i+t_P), \qquad (37)\\
&= d\hat{\tilde{\tilde{t}}}^s(t_i)+\dot{\hat{\tilde{\tilde{t}}}}^s(t_i)\cdot t_P+\hat{\tilde{\tilde{\delta}}}_{,j}^s(t_i)+\mu_j\hat{\tilde{\tilde{\imath}}}_u^s(t_i),\\
&= \hat{\tilde{\tilde{\omega}}}_{u,j}^s(t_i)+\dot{\hat{\tilde{\tilde{t}}}}^s(t_i)\cdot t_P,
\end{aligned}$$

where $\hat{\tilde{\omega}}_{u,j}^s$ and $\hat{\tilde{\tilde{\omega}}}_{u,j}^s$ represent the estimated user-specific combined network corrections without and with the satellite clock model, respectively. From Table 2, we see that the estimable between-satellite clock rates (applying satellite clock model) are equal to the original between-satellite clock rates:

$$\dot{\tilde{\tilde{t}}}^{1s}=\dot{t}^{1s}. \qquad (38)$$

Fig. 7 shows the estimated between-satellite clock rates without and with clock models

for the satellite pair G07 and G09 from 14:00 to 15:00 on March 28, 2017. The yellow line represents the between-satellite clock rates generated by fitting polynomials using the $\hat{\dot{t}}^s$ of the last 10 s (see Eq. (35)). The blue line represents the between-satellite clock rates for the same satellite pair and the same time interval computed using the IGS final satellite clocks (IGS clock 2017) with a sampling interval of 30 s:

$$\begin{aligned} \dot{\hat{t}}^{1s}_{IGS}(t_i) &= \dot{\hat{t}}^{s}_{IGS}(t_i) - \dot{\hat{t}}^{1}_{IGS}(t_i) \\ &= \frac{\hat{dt}^{s}_{IGS}(t_{i+1}) - \hat{dt}^{s}_{IGS}(t_i)}{\Delta t_{i+1}} - \frac{\hat{dt}^{1}_{IGS}(t_{i+1}) - \hat{dt}^{1}_{IGS}(t_i)}{\Delta t_{i+1}}, \end{aligned} \tag{39}$$

where $\hat{dt}^{s}_{IGS}(t_i)$ represents the IGS clock bias for satellite s at t_i. The time difference Δt_{i+1} amounts to 30 s by calculating the IGS between-satellite clock rates.

Based on the results generated using the IGS satellite clocks (see the blue line in Fig. 7), we assume that the between-satellite clock rates for the satellites G07 and G09 from 14:00 to 15:00 on March 28, 2017 vary within millimetres per second. Applying strong satellite clock constraints helps to reduce the noise in the estimates of the between-satellite clock rates. The yellow line, which represents the estimates of the between-satellite clock rates obtained by fitting polynomials (see Eq. 35), has shown the most noisy behaviours among all the different choices. Based on Eq. (20), we see that the between-satellite clock rates obtained by fitting polynomials ($\dot{\hat{dt}}^{1s}$) include not only the original between-satellite clock rates ($\dot{dt}^{1s}$), but also the rates of the term $g_1^{1s}\tau_1(t_1)$. However, the rate of the term $g_1^{1s}\tau_1(t_1)$ for the satellite pair G07 and G09 during this time interval varies within tens of micrometres per second. The noisy behaviour of the yellow line in Fig. 7 is caused by the noisy behaviour of the between-satellite clock estimates without clock constraint (see the blue line in Fig. 4).

For the relevant satellites in the predicted test time intervals, the between-satellite clock rates computed using the IGS clocks (IGS clock 2017) all have small amplitudes (from sub-mm/s or even less to mm/s). In case of not applying satellite clock model, we thus also test the option to directly set the predicted satellite clocks at $t_i + t_P$ to those at t_i. In other words,

apart from obtaining the values of $\dot{\hat{dt}}^s$ by fitting polynomials (see Eq. (35)), the values of the $\dot{\hat{dt}}^s$ can also be directly set to 0 m/s. In section "Latency and user positioning results", for the case without satellite clock model, both options, i.e., obtaining the satellite clock rates by fitting polynomials and directly setting them to 0 m/s, are tested.

Apart from the between-satellite clock rate, the prediction time t_P, which varies according to the latency of the network corrections, also influences the predicted combined corrections (see Eqs. (36) and (37)). The residuals of the predicted between-satellite combined network corrections without ($\Delta\check{\tilde{\omega}}^{1s}_{u,j}$) and with satellite clock models ($\Delta\check{\tilde{\omega}}^{1s}_{u,j}$) are defined as (see also Eq. (28)):

$$\Delta\check{\tilde{\omega}}^{1s}_{u,j}(t_i + t_P) = \check{\tilde{\omega}}^{1s}_{u,j}(t_i + t_P) - \hat{p}^{1s}_1 \cdot (t_i + t_P - t_0) - \hat{p}^{1s}_0, \quad (40)$$

$$\Delta\check{\tilde{\omega}}^{1s}_{u,j}(t_i + t_P) = \check{\tilde{\omega}}^{1s}_{u,j}(t_i + t_P) - \hat{p}^{1s}_1 \cdot (t_i + t_P - t_0) - \hat{p}^{1s}_0. \quad (41)$$

Fig. 8 shows the residuals of the predicted between-satellite combined network corrections without and with applying different satellite clock constraints with the same prediction time t_P of 3 s (see Fig. 8(a)) and with different prediction time t_P applying the same clock constraint $q_{dt^s} = 7$ mm/$\sqrt{\text{s}}$ (see Fig. 8(b)) for user station PKVL from 14:00 to 15:00 on March 28, 2017. The yellow line in Fig. 8(a) represents the case using $\dot{\hat{dt}}^s$ obtained by fitting polynomials (see Eq. (35)). As shown in Fig. 8, the predicted combined corrections are influenced by both the satellite clock constraint and the prediction time t_P.

To compare the predicted and the estimated network corrections, the differences of the predicted (see Eqs. (33) and (34)) and the estimated between-satellite clocks without and with satellite clock model are plotted in Fig. 9(a) for a latency of 3 s, and those for the between-satellite combined network corrections (see Eqs. (36) and (37)) are plotted in Fig. 9(b). Without satellite clock model (see the yellow lines in Fig. 9), the satellite clock rates are obtained by fitting polynomials (see Eq. (35)). We see that for both the between-satellite clocks and combined network corrections, applying strong satellite clock models

(with q_{dt^s} of 1 and 0.5 mm/$\sqrt{\text{s}}$) helps to reduce the differences between the predictions and the estimations.

Applying satellite clock model with q_{dt^s} of 0.5 mm/$\sqrt{\text{s}}$, Fig. 10 shows also the differences of the predicted and the estimated combined network corrections with a latency of 3, 6 and 10 s. The differences are enlarged with increasing latency of the network products.

LATENCY AND USER POSITIONING RESULTS

Due to the time delay of the network products, the estimated satellite clocks, satellite phase biases and the interpolated user-specific ionospheric delays are predicted with a latency ranging from 3 to 10 s and are provided to the users. For reason of comparison, we also computed predictions without satellite clock model. The satellite clock rates can be computed by fitting polynomials using the satellite clock estimates $\hat{\hat{dt}}^s$ without satellite clock model of the last 10 s (see Eq. (35)). Since the network corrections are effective on between-satellite level for user positioning (Khodabandeh and Teunissen 2015), and based on the fact that the between-satellite clock rates (obtained using IGS clocks) for the tested time intervals have small amplitudes (sub-mm/s to mm/s, see the previous section), we also tested the option to directly set the values of the satellite clock rates ($\dot{\hat{\hat{dt}}}^s$ in Eq. (34)) to 0 m/s in case that no satellite clock model is applied.

In this study, the station coordinates in the daily final solution provided by Geoscience Australia (GA) are used as ground truth. The same as in the network processing, the zenith-referenced a priori standard deviations of the phase and the code observations are set to be 3 mm and 3 dm, respectively. The receiver hardware biases and the ZTDs are time-linked with a spectral density of 1 m/$\sqrt{\text{s}}$ and 0.1 mm/$\sqrt{\text{s}}$, respectively. The receiver coordinates are estimated kinematically without link in time.

Fig. 11 shows the coordinate differences for user station PKVL using the predicted network corrections (with a q_{dt^s} of 0.5 mm/$\sqrt{\text{s}}$ and a latency of 3, 6 and 10 s) and the estimated network corrections in the North-, East- and Up-directions from 14:00 to 15:00 on March 28, 2017. The y-axis is scaled to -5 and 5 cm for the horizontal coordinates, and to -2 and 2 dm

for the vertical coordinates. The results are based on partial ambiguity resolution with a pre-defined success rate of 99.99%. We see that the coordinate differences increase with the increasing latency in all the three directions.

In order to compare the influences of different sets of the predicted network corrections on the user positioning results for different users in different time intervals, the overall RMS of the coordinate increments are computed using the coordinate increments (with respect to the ground truth) of both user stations from 6:00 to 7:00, from 14:00 to 15:00 and from 22:00 to 23:00 (in GPST) on March 28, 2017 with a latency ranging from 3 to 10 s. The overall RMS is defined as:

$$\sigma_x = \sqrt{\frac{\sum_{h=1}^{T}\sum_{u=1}^{U}\sum_{i=N_s}^{N_e} x_{u,h}^2(t_i)}{T \cdot U \cdot (N_e - N_s + 1)}}, \tag{42}$$

where T and U represent the number of the tested time intervals and the number of the user stations, respectively. N_s and N_e represent the starting and the ending time epoch for calculating the RMS of the user positioning results, respectively. $x_{u,h}(t_i)$ denotes the coordinate increment (with respect to the ground truth) for the user station u of the time interval h at the time point t_i based on partial ambiguity resolution. The RMS in the North-, East- and Up-direction are denoted as $\hat{\sigma}_N$, $\hat{\sigma}_E$ and $\hat{\sigma}_U$, respectively. The first 10 s are considered as the filter initialization time and are not used for computing the RMS of the coordinates.

Fig. 12 shows the overall RMS of the North-, East- and Up-coordinates applying different prediction methods for different latencies of the network products. The value 0 in the x-axis represents the case without latency, i.e., using the estimated network corrections. The legend "No model ($\dot{\tilde{d}}\tilde{t}^s$=0 m/s)" represents the case where the values of the satellite clock rate are directly set to be 0 m/s, and the legend "No model (Polyfit)" represents the case where the satellite clock rates are computed by fitting polynomials using the satellite clock estimates without clock model of the last 10 s (see Eq. (35)).

From Fig. 12 we see that estimation of satellite clock rates by fitting polynomials (see the

yellow lines in Fig. 12) degrades the user positioning results significantly already by short latencies, e.g., 3 s. Directly setting the values of the satellite clock rates to 0 m/s avoids the noisy behaviours of the between-satellite clock rates in Fig. 7. However, the fact that the between-satellite clock rates are not 0 m/s increases the biases in the predicted between-satellite combined network corrections with the increasing latencies. For long latencies, e.g., larger than 8 s, large degradation in the user positioning results can thus occur. Using the satellite clock rates with weak satellite clock models, i.e., with $q_{dt^s} = 7$ mm/$\sqrt{\text{s}}$ (see the red lines in Fig. 7 and 12) does not generate better results compared to the case where we directly set the $\dot{\hat{\tilde{t}}}^s$ to 0 m/s (see the blue lines in Fig. 12), especially in the vertical direction. However, by strengthening the constraint in satellite clock model, the noise in the between-satellite clock rates are significantly reduced (see the green and the magenta lines in Fig. 7). This leads to improvements in all the three directions of the user positioning results (see the green and the magenta lines in Fig. 12). Compared to the yellow and the blue lines without satellite clock model, the benefits are especially large for long latencies with t_P larger than 8 s. Applying strong satellite clock constraint, i.e., with a q_{dt^s} of 0.5 or 1 mm/$\sqrt{\text{s}}$, the RMS of the coordinates are reduced within centimetres to decimetres for a latency larger than 6 s, compared to the cases without satellite clock model.

CONCLUSION

This contribution studies the estimability of the parameters applying dynamic satellite clock model in the network PPP-RTK processing under *single*-frequency and ionosphere-weighted scenario. With dynamic satellite clock models incorporated in the network Kalman filter, we developed a single-frequency network full-rank model applicable to an arbitrary GNSS. In order to test the implementation of the satellite clock model, real data from a small-scale network in 3 different time intervals are used to compute the estimated and the predicted network corrections (the estimable satellite clocks, satellite phase biases and ionospheric delays). The estimated and the predicted network corrections are provided to the users, and the influences of the satellite clock models on the user positioning results are

studied and discussed with respect to their RMS (deviated from the ground truth) for a latency ranging from 3 to 10 s. Predictions without satellite clock models are also performed for reason of comparison.

In this study, it was found that the estimated combined network corrections do not benefit much from satellite clock models. However, modelling satellite clocks is shown to be beneficial to reduce the noise in the *predicted* between-satellite combined network corrections in case of latencies of the network products. These improvements are also reflected in the user positioning results. Without satellite clock model, the results are computed both by directly setting the values of the satellite clock rates to 0 m/s and by fitting polynomials using the satellite clock estimates without constraint of the last 10 s. The latter case already generates dm-level RMS in all the three directions at short latency of 3 s. Directly setting the values of the satellite clock rates to 0 m/s also leads to dm-level RMS in all the three directions at long latency larger than 8 s. Applying a strong satellite clock model for GPS satellites with, e.g., q_{dt^s} equals to 0.5 or 1 mm/$\sqrt{\text{s}}$, the RMS of the user coordinates are reduced within centimetres to decimetres for latencies larger than 6 s. Compared to the discussed prediction methods without satellite clock model, advantages of the strong satellite clock models in single-frequency PPP-RTK network processing are directly reflected in user positioning results, especially in cases of long latencies of the network products.

ACKNOWLEDGEMENTS

We would like to thank the IGS, Geoscience Australia (GA) and Vicmap Position - GPSnet (Victoria State Government) to provide the orbit and the clock products, the precise coordinates and the observation data of the stations on their servers. We would also like to thank our colleagues in the GNSS Research Centre, Curtin University, for their contributions on the development of the Curtin PPP-RTK Software. PJG Teunissen is recipient of an Australian Research Council (ARC) Federation Fellowship (project number FF0883188).

REFERENCES

569 Allan, D. W. (1987). "Time and Frequency (Time-Domain) Characterization, Estimation,
570 and Prediction of Precision Clocks and Oscillators." *IEEE T. Ultrason. Ferr.*, 34(6), 647–
571 654.

572 Baarda, W. (1981). *S-transformations and criterion matrices, in Publications on geodesy*
573 *(Vol. 5, Nr. 1)*. Netherlands Geodetic Commission, Delft, the Netherlands, second revised
574 edition.

575 Banville, S., Collins, P., Zhang, W., and Langley, R. B. (2014). "Global and Regional Iono-
576 spheric Corrections for Faster PPP Convergence." *Navigation: Journal of The Institute of*
577 *Navigation*, 61(2), 115–124.

578 Bevis, M., Businger, S., Herring, T., Rocken, C., Anthes, R., and Ware, R. (1992). "GPS
579 meteorology: Sensing of atmospheric water vapor using the Global Positioning System."
580 *J. Geophys. Res.*, 97, 15787–15801.

581 Collins, P. (2008). "Isolating and Estimating Undifferenced GPS Integer Ambiguities." *Proc.,*
582 *the 2008 National Technical Meeting of The Institute of Navigation*, San Diego, CA, 720–
583 732.

584 Dach, R., Hugentobler, U., Fridez, P., and Meindl, M. (2007). *Bernese GNSS Software*
585 *Version 5.0. User manual*. Astronomical Institute, University of Bern.

586 Dow, J. M., Neilan, R. E., and Rizos, C. (2009). "The International GNSS Service in a
587 changing landscape of Global Navigation Satellite Systems." *J. Geodesy*, 83(3–4), 191–
588 198.

589 Eueler, H. J. and Goad, C. C. (1991). "On optimal filtering of GPS dual frequency observa-
590 tions without using orbit information." *B. Geod.*, 65(2), 130–143.

591 Ge, M., Gendt, G., Rothacher, M., Shi, C., and Liu, J. (2008). "Resolution of GPS carrier-
592 phase ambiguities in Precise Point Positioning (PPP) with daily observations." *J. Geodesy*,
593 82(7), 389–399.

594 Geng, J., Teferle, F. N., Meng, X., and Dodson, A. H. (2011). "Towards PPP-RTK: Ambigu-
595 ity resolution in real-time precise point positioning." *Adv. Space Res.*, 47(10), 1664–1673.

596 Geoscience Australia (2017). "Data from the Geoscience Australia", <www.ga.gov.au>
597 (May, 2017).

598 Google earth 7.0.3.8542 (2017). "Google earth imagery" (October 18, 2017). Victoria, Aus-
599 tralia. 37°47'13.50"S, 144°58'57.07"E, Eye alt 66.19 km. TerraMetrics 2017. DigitalGlobe
600 2017, <https://www.google.com/earth/> (December, 2017).

601 Hauschild, A. and Montenbruck, O. (2009). "Kalman-filter-based GPS clock estimation for
602 near real-time positioning." *GPS Solut.*, 13(3), 173–182.

603 Hofmann-Wellenhof, B., Lichtenegger, H., and Wasle, E. (2008). *GNSS–Global Navigation*
604 *Satellite Systems: GPS, GLONASS, Galileo, and more*. Springer-Verlag, Wien.

605 Huisman, L., Teunissen, P. J. G., and Hu, C. (2012). "GNSS precise point positioning in
606 regional reference frames using real-time broadcast corrections." *J. Appl. Geodesy*, 6(1),
607 15–23.

608 IGS clock (2017). "International GNSS Service, GNSS Final Combined Satellite and Receiver
609 Clock Solution (30 second) Product", Greenbelt, MD, USA:NASA Crustal Dynamics Data
610 Information System (CDDIS), <ftp://cddis.gsfc.nasa.gov/> (June, 2017).

611 Khodabandeh, A. and Teunissen, P. J. G. (2015). "An analytical study of PPP-RTK correc-
612 tions: precision, correlation and user-impact." *J. Geodesy*, 89(11), 1109–1132.

613 Laurichesse, D. and Mercier, F. (2007). "Integer Ambiguity Resolution on Undifferenced
614 GPS Phase Measurements and its Application to PPP." *Proc., ION GNSS 2007*, Fort
615 Worth, TX, 839–848.

616 Laurichesse, D., Mercier, F., and Berthias, J. P. (2010). "Real-time PPP with Undifferenced
617 Integer Ambiguity Resolution, Experimental Results." *Proc., ION GNSS 2010*, Portland,
618 OR, 2534–2544.

619 Leandro, R., Landau, H., Nitschke, M., Glocker, M., Seeger, S., Chen, X., Deking, A.,
620 BenTahar, M., Zhang, F., Ferguson, K., Stolz, R., Talbot, N., Lu, G., Allison, T., Brandl,
621 M., Gomez, V., Cao, W., and Kipka, A. (2011). "RTX Positioning: The Next Generation
622 of cm-accurate Real-time GNSS Positioning." *Proc., ION GNSS 2011*, Portland, OR,

1460–1475.

Li, W., Nadarajah, N., Teunissen, P. J. G., Khodabandeh, A., and Chai, Y. (2017). "Array-Aided Single-Frequency State-Space RTK with Combined GPS, Galileo, IRNSS, and QZSS L5/E5a Observations." *J. Surv. Eng.*, 143(4), 10.1061/(ASCE)SU.1943–5428.0000227, 04017006.

Loyer, S., Perosanz, F., Mercier, F., Capdeville, H., and Marty, J. C. (2012). "Zero-difference GPS ambiguity resolution at CNES-CLS IGS Analysis Center." *J. Geodesy*, 86(11), 991–1003.

Odijk, D. (2002). "Fast precise GPS positioning in the presence of ionospheric delays." Ph.D. thesis, Delft University of Technology, Delft, the Netherlands, <https://repository.tudelft.nl/islandora/object/uuid:40d49779-2ef4-4641-9ae4-f591871063fa?collection=research> (December, 2017).

Odijk, D., Arora, B. S., and Teunissen, P. J. G. (2014a). "Predicting the Success Rate of Long-baseline GPS+Galileo (Partial) Ambiguity Resolution." *The Journal of Navigation*, 67(3), 385–401.

Odijk, D., Khodabandeh, A., Nadarajah, N., Choudhury, M., Zhang, B., Li, W., and Teunissen, P. J. G. (2017). "PPP-RTK by means of S-system theory: Australian network and user demonstration." *J. Spat. Sci.*, 62(1), 3–27.

Odijk, D., Teunissen, P. J. G., and Huisman, L. (2012a). "First results of mixed GPS-GIOVE single-frequency RTK in Australia." *J. Spat. Sci.*, 57(1), 3–18.

Odijk, D., Teunissen, P. J. G., and Khodabandeh, A. (2014b). "Single-Frequency PPP-RTK: Theory and Experimental Results." *Earth on the Edge: Science for a Sustainable Planet. IAG Symposia, vol 139*, C. Rizos and P. Willis, eds., Springer, Berlin, Heidelberg, 571–578.

Odijk, D., Teunissen, P. J. G., and Zhang, B. (2012b). "Single-Frequency Integer Ambiguity Resolution Enabled GPS Precise Point Positioning." *J. Surv. Eng.*, 138(4), 10.1061/(ASCE)SU.1943–5428.0000085, 193–202.

Odolinski, R. and Teunissen, P. J. G. (2017). "Low-cost, high-precision, single-frequency

GPS-BDS RTK positioning." *GPS Solut.*, 21(3), 1315–1330.

Riley, W. J. (2008). *Handbook of Frequency Stability Analysis*. NIST Special Publication 1065.

Saastamoinen, J. (1972). "Contribution to the theory of atmospheric refraction." *Bull. Geod.*, 105(1), 279–298.

Senior, K. L., Ray, J. R., and Beard, R. L. (2008). "Characterization of periodic variations in the GPS satellite clocks." *GPS Solut.*, 12(3), 211–225.

Springer, T. A. and Hugentobler, U. (2001). "IGS ultra rapid products for (near-) real-time applications." *Physics and Chemistry of the Earth, Part A: Solid Earth and Geodesy*, 26(6–8), 623–628.

Teunissen, P. J. G. (1985). "Zero Order Design: Generalized Inverses, Adjustment, the Datum Problem and S-Transformations." *Optimization and Design of Geodetic Networks*, E. W. Grafarend and F. Sansò, eds., Springer, Berlin, Heidelberg, 11–55.

Teunissen, P. J. G. and Khodabandeh, A. (2015). "Review and principles of PPP-RTK methods." *J. Geodesy*, 89(3), 217–240.

Teunissen, P. J. G. and Montenbruck, O. (2017). *Springer Handbook of Global Navigation Satellite Systems*. Springer International Publishing.

Teunissen, P. J. G., Odijk, D., and Zhang, B. (2010). "PPP-RTK: Results of CORS Network-Based PPP with Integer Ambiguity Resolution." *Journal of Aeronautics, Astronautics and Aviation, Series A*, 42(4), 223–230.

van Bree, R. J. P. and Tiberius, C. C. J. M. (2012). "Real-time single-frequency precise point positioning: accuracy assessment." *GPS Solut.*, 16(2), 259–266.

van Dierendonck, A. J., McGraw, J. B., and Brown, R. G. (1984). "Relationship between Allan variances and Kalman filter parameters." *Proc., PTTI 1984*, Greenbelt, MD, 273–293.

Wang, K., Khodabandeh, A., and Teunissen, P. J. G. (2017). "A study on predicting network corrections in PPP-RTK processing." *Adv. Space Res.*, 60(7), 1463–1477.

677 Wübbena, G., Schmitz, M., and Bagge, A. (2005). "PPP-RTK: Precise Point Positioning Us-
678 ing State-Space Representation in RTK Networks." *Proc., ION GNSS 2005*, Long Beach,
679 CA, 2584–2594.
680 Younes, S. A. M. (2016). "Modeling investigation of wet tropospheric delay error and pre-
681 cipitable water vapor content in Egypt." *The Egyptian Journal of Remote Sensing and*
682 *Space Science*, 19(2), 333–342.
683 Yu, X. and Gao, J. (2017). "Kinematic Precise Point Positioning Using Multi-Constellation
684 Global Navigation Satellite System (GNSS) Observations." *ISPRS Int. J. Geo-Inf.*, 6(1),
685 6.

List of Tables

1 Estimable parameters and S-basis parameters in Eqs. (4) and (5) with the ionospheric delays, the hardware biases and the ZTDs linked in time (as random-walk process) for *single*-frequency ionosphere-weighted scenario *without* satellite clock model). *Relative* ZTDs between stations are estimated. . . 30

2 Changed estimable parameters *with* the satellite clock model (see Eq. (7)) with the ionospheric delays, the hardware biases and the ZTDs linked in time (as random-walk process) for *single*-frequency ionosphere-weighted scenario. *Absolute* ZTDs are estimated for each station. 31

3 Settings of the dynamic model in the network Kalman filter. Parameters not listed in this Table are estimated as unlinked parameters. 32

Table 1. Estimable parameters and S-basis parameters in Eqs. (4) and (5) with the ionospheric delays, the hardware biases and the ZTDs linked in time (as random-walk process) for *single*-frequency ionosphere-weighted scenario *without* satellite clock model). *Relative* ZTDs between stations are estimated.

Parameter	Interpretation
$\tilde{\tau}_{r\neq 1}(t_1)$	$\tau_r(t_1) - \tau_1(t_1)$
$\tilde{\tau}_r(t_{i>1})$	$\tau_r(t_i) - \tau_1(t_1)$
$\tilde{dt}_{r\neq 1}(t_i)$	$dt_{1r}(t_i) + d_{1r,j}(t_1)$
$\tilde{dt}^s(t_i)$	$dt^s(t_i) + d^s_{,j}(t_1) - (dt_1(t_i) + d_{1,j}(t_1)) - g^s_1(t_i)\tau_1(t_1) - \mu_j \iota^s_1(t_1)$
$\tilde{\iota}^s_r(t_i)$	$\iota^s_r(t_i) - \iota^s_1(t_1), \begin{cases} r \neq 1, i = 1 \\ \forall r, i > 1 \end{cases}$
$\tilde{\delta}_{r,j}(t_i)$	$\delta_{r,j}(t_i) - \delta_{1,j}(t_1) - d_{1r,j}(t_1) + z^1_{1r,j}\lambda_j, \begin{cases} r \neq 1, i = 1 \\ \forall r, i > 1 \end{cases}$
$\tilde{\delta}^s_{,j}(t_i)$	$\delta^s_{,j}(t_i) - \delta_{1,j}(t_1) - (d^s_{,j}(t_1) - d_{1,j}(t_1)) + 2\mu_j \iota^s_1(t_1) - z^s_{1,j}\lambda_j$
$\tilde{d}_{r,j}(t_{i>1})$	$d_{r,j}(t_i) - d_{r,j}(t_1)$
$\tilde{d}^s_{,j}(t_{i>1})$	$d^s_{,j}(t_i) - d^s_{,j}(t_1)$
$\tilde{z}^{s\neq 1}_{r\neq 1,j}$	$z^s_{1r,j} - z^1_{1r,j}$
S-basis	$\tau_1(t_1), dt_1(t_i), \delta_{1,j}(t_1), d_{r,j}(t_1), d^s_{,j}(t_1), \iota^s_1(t_1), z^s_{1,j}, z^1_{r,j}$

Table 2. Changed estimable parameters *with* the satellite clock model (see Eq. (7)) with the ionospheric delays, the hardware biases and the ZTDs linked in time (as random-walk process) for *single*-frequency ionosphere-weighted scenario. *Absolute* ZTDs are estimated for each station.

Parameter	Interpretation
$\tilde{\tilde{\tau}}_r(t_i)$	$\tau_r(t_i)$
$d\tilde{\tilde{t}}_r(t_i)$	$dt_r(t_i) + d_{1r,j}(t_1) - dt_1(t_1) - \frac{t_i - t_1}{\Delta t_2}(dt_1(t_2) - dt_1(t_1)), \begin{cases} r \neq 1, i = 1, 2 \\ \forall r, i > 2 \end{cases}$
$d\tilde{\tilde{t}}^s(t_i)$	$dt^s(t_i) + d^s_{,j}(t_1) - (dt_1(t_1) + d_{1,j}(t_1)) - \mu_j \iota^s_1(t_1) - \frac{t_i - t_1}{\Delta t_2}(dt_1(t_2) - dt_1(t_1))$
$\dot{d}\tilde{\tilde{t}}^s(t_{i>2})$	$\dot{dt}^s(t_i) - \frac{1}{\Delta t_2}(dt_1(t_2) - dt_1(t_1))$

Table 3. Settings of the dynamic model in the network Kalman filter. Parameters not listed in this Table are estimated as unlinked parameters.

Paramter	Process noise
Receiver hardware delays	1 m/$\sqrt{\text{s}}$
Satellite hardware delays	0.01 m/$\sqrt{\text{s}}$
ZTDs	0.1 mm/$\sqrt{\text{s}}$
Ionospheric delays	0.5 m/$\sqrt{\text{s}}$
Satellite clocks	unlinked, 7, 1, 0.5 mm/$\sqrt{\text{s}}$
Ambiguities	0 m/$\sqrt{\text{s}}$

List of Figures

1 Flowcharts of the number of the observations equations (including the constraint equations, denoted as l_o), the number of the estimable parameters (l_u) and the number of the redundancies (l_r) without satellite clock model and the addition in numbers after applying the satellite clock model (see Tables 1 and 2), which is marked with blue. t_1 and t_2 represent the first and the second time epochs of the processing, respectively, and $t_{i>1}$ and $t_{i>2}$ represent the time after the first and the second epochs, respectively. n and m represent the number of the receivers and the satellites at the corresponding epoch, respectively. 36

2 Local network for the network and the user processing on March 28, 2017. The network and the user stations are represented by the yellow and the red marks, respectively. The inter-station distance of the network stations ranges from 19.6 to 42.9 km. The map is generated using Google earth 7.0.3.8542 (2017). 37

3 (a) Between-satellite differences of the mapping functions for ZTDs and (b) $\tau_1(t_1)$ obtained with Eq. (22) for the satellite pairs G07-G09, G07-G30, G07-G23 and G07-G27 from 14:00 to 15:00 on March 28, 2017. The reference station (station 1) is station DORA (see Fig. 2). 38

4 Formal standard deviations of the estimable between-satellite clocks without and with satellite clock model for satellites G07 and G09 from 14:00 to 15:00 (in GPST) on March 28, 2017. 39

5 (a) Formal standard deviations of the between-satellite combined network corrections (see Eqs. (23) and (24)) for the network station WBEE without and with satellite clock models and (b) the correlation coefficients between $d\tilde{t}^{1s}$ (or $d\tilde{\tilde{t}}^{1s}$) and $\tilde{\varphi}^{1s}_{r,j}$ (for the network station WBEE, see Eq. (25)) for the satellites G07 and G09 from 14:00 to 15:00 on March 28, 2017. 40

6 (a) The residual between-satellite combined network corrections (see Eqs. (26) and (27)) and (b) those after adding the O-C terms of the phase observations (see Eqs. (29) and (30)) of station WBEE for satellites G07 and G09 without and with satellite clock models from 14:00 to 15:00 on March 28, 2017. . . . 41

7 Estimates of the between-satellite clock rates for satellites G07 and G09 from 14:00 to 15:00 on March 8, 2017. The yellow line represents the estimates of the between-satellite clock rates obtained by fitting polynomials (see Eq. (35)). The blue line represents the estimates of the between-satellite clock rates computed using the IGS final clock products (see Eq. (39)). 42

8 Residuals of the predicted between-satellite combined network corrections (see Eqs. (40) and (41)) for user station PKVL and the satellites G07 and G09 from 14:00 to 15:00 on March 28, 2017 (a) without and with applying different satellite clock constraints with a prediction time of 3 s and (b) applying a satellite clock model of $q_{dt^s} = 7$ mm/$\sqrt{\text{s}}$ with different prediction time. . . . 43

9 Differences of (a) the predicted and estimated between-satellite clocks (see Eqs. (33) and (34)) and (b) the predicted and estimated between-satellite combined network corrections (see Eqs. (36) and (37)) for G07 and G09 and user station PKVL from 14:00 to 15:00 on March 28, 2017. The latency in case of prediction is 3 s. 44

10 Differences of the predicted and estimated between-satellite combined network corrections (see Eqs. (36) and (37)) for G07 and G09 and user station PKVL from 14:00 to 15:00 on March 28, 2017 applying satellite clock model with q_{dt^s} of 0.5 mm/$\sqrt{\text{s}}$ and latencies of 3, 6 and 10 s. 45

11 Coordinate differences for user station PKVL using predicted network corrections (with a q_{dt^s} of 0.5 mm/$\sqrt{\text{s}}$ and a latency of 3, 6 and 10 s) and estimated network corrections in the North-, East- and Up-directions from 14:00 to 15:00 on March 28, 2017. The y-axis is scaled to -5 and 5 cm for the horizontal coordinates, and to -2 and 2 dm for the vertical coordinates. The results are based on partial ambiguity resolution with a pre-defined success rate of 99.99%. 46

12 The overall RMS of the North-, East- and Up-coordinate increments (with respect to the ground truth) using the estimated and the predicted network corrections from 6:00 to 7:00, from 14:00 to 15:00 and from 22:00 to 23:00 (in GPST) on March 28, 2017 with a latency ranging from 3 to 10 s based on partial ambiguity resolution. The yellow and the blue lines represent the cases using the $\dot{\hat{\tilde{t}}}^s$ obtained by post fitting polynomials (see Eq. (35)) and directly setting the values to 0 m/s, respectively. The red, the green and the magenta lines represent the cases using $\dot{\hat{\tilde{t}}}^s$ obtained by modelling satellite clocks in the network Kalman filter with q_{dt^s} of 7, 1 and 0.5 mm/$\sqrt{\text{s}}$, respectively. 47

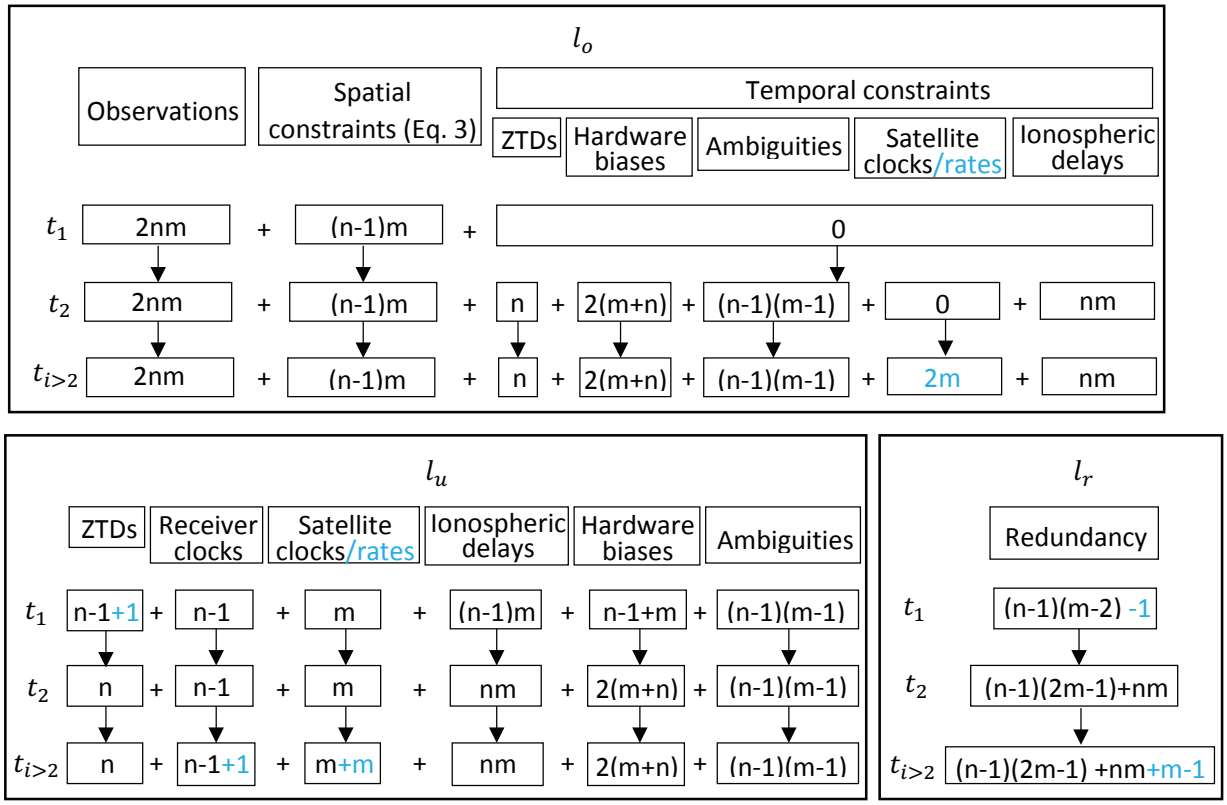

Fig. 1. Flowcharts of the number of the observations equations (including the constraint equations, denoted as l_o), the number of the estimable parameters (l_u) and the number of the redundancies (l_r) without satellite clock model and the addition in numbers after applying the satellite clock model (see Tables 1 and 2), which is marked with blue. t_1 and t_2 represent the first and the second time epochs of the processing, respectively, and $t_{i>1}$ and $t_{i>2}$ represent the time after the first and the second epochs, respectively. n and m represent the number of the receivers and the satellites at the corresponding epoch, respectively.

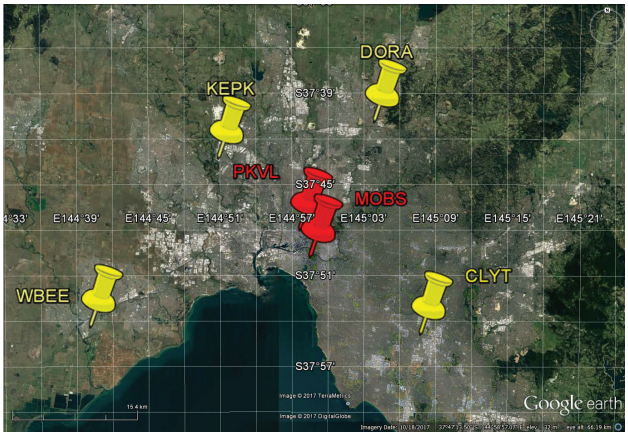

Fig. 2. Local network for the network and the user processing on March 28, 2017. The network and the user stations are represented by the yellow and the red marks, respectively. The inter-station distance of the network stations ranges from 19.6 to 42.9 km. The map is generated using Google earth 7.0.3.8542 (2017).

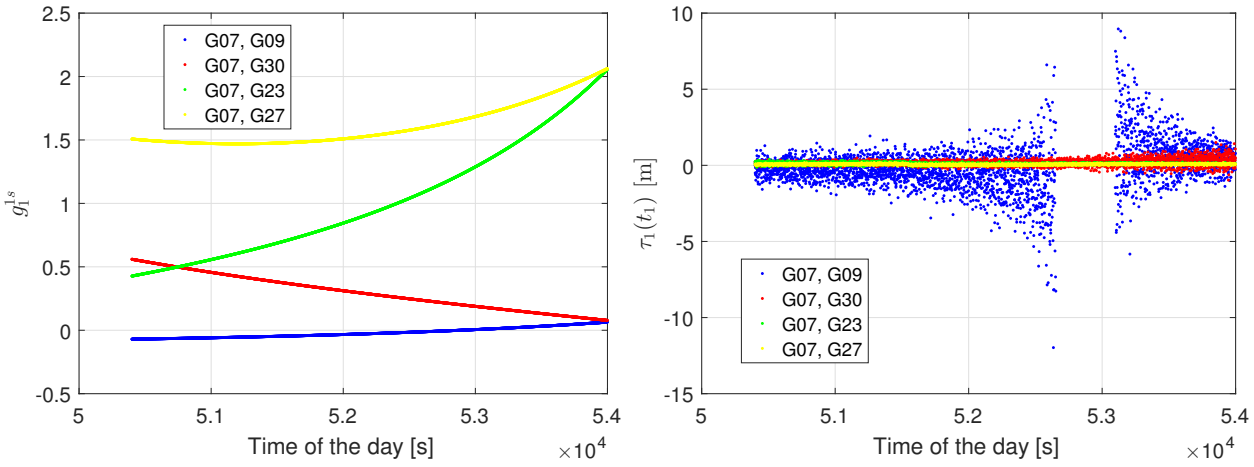

(a) g_1^{1s} (b) $\tau_1(t_1)$

Fig. 3. (a) Between-satellite differences of the mapping functions for ZTDs and (b) $\tau_1(t_1)$ obtained with Eq. (22) for the satellite pairs G07-G09, G07-G30, G07-G23 and G07-G27 from 14:00 to 15:00 on March 28, 2017. The reference station (station 1) is station DORA (see Fig. 2).

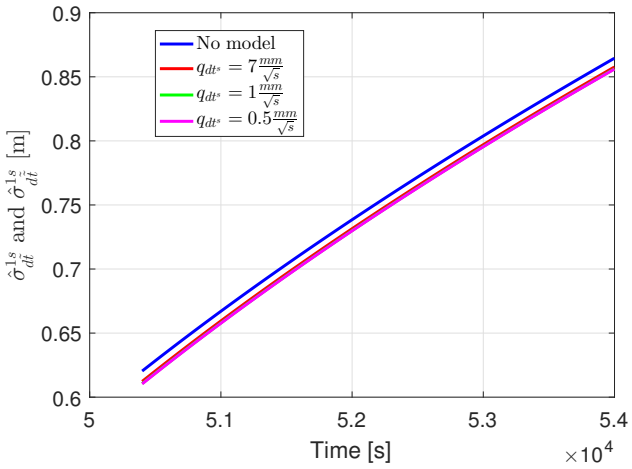

Fig. 4. Formal standard deviations of the estimable between-satellite clocks without and with satellite clock model for satellites G07 and G09 from 14:00 to 15:00 (in GPST) on March 28, 2017.

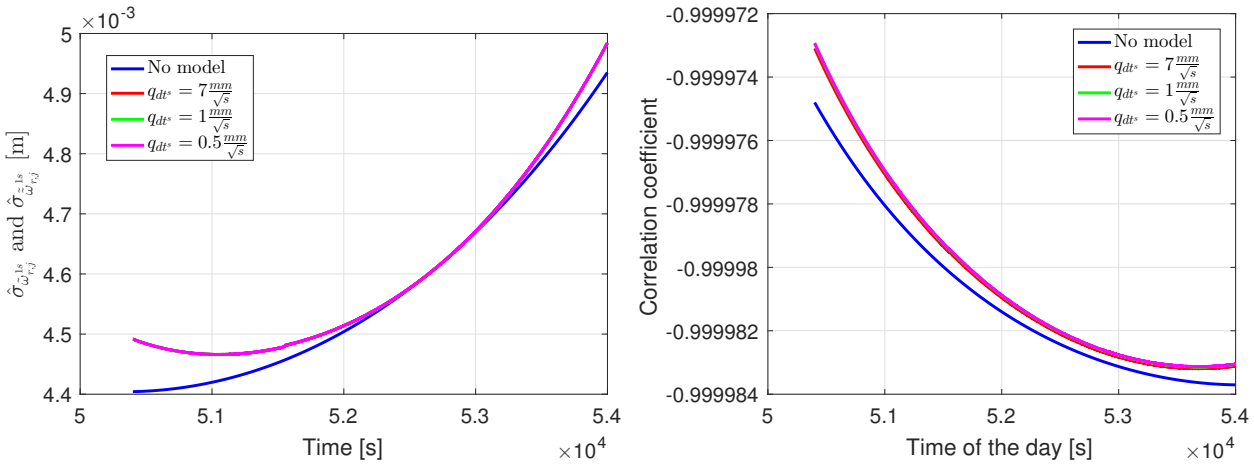

(a) $\hat{\sigma}_{\tilde{\omega}^{1s}_{r,j}}$ and $\hat{\sigma}_{\tilde{\tilde{\omega}}^{1s}_{r,j}}$ (G07 and G09)

(b) Correlation coefficient (G07 and G09)

Fig. 5. (a) Formal standard deviations of the between-satellite combined network corrections (see Eqs. (23) and (24)) for the network station WBEE without and with satellite clock models and (b) the correlation coefficients between $d\tilde{t}^{1s}$ (or $d\tilde{\tilde{t}}^{1s}$) and $\tilde{\varphi}^{1s}_{r,j}$ (for the network station WBEE, see Eq. (25)) for the satellites G07 and G09 from 14:00 to 15:00 on March 28, 2017.

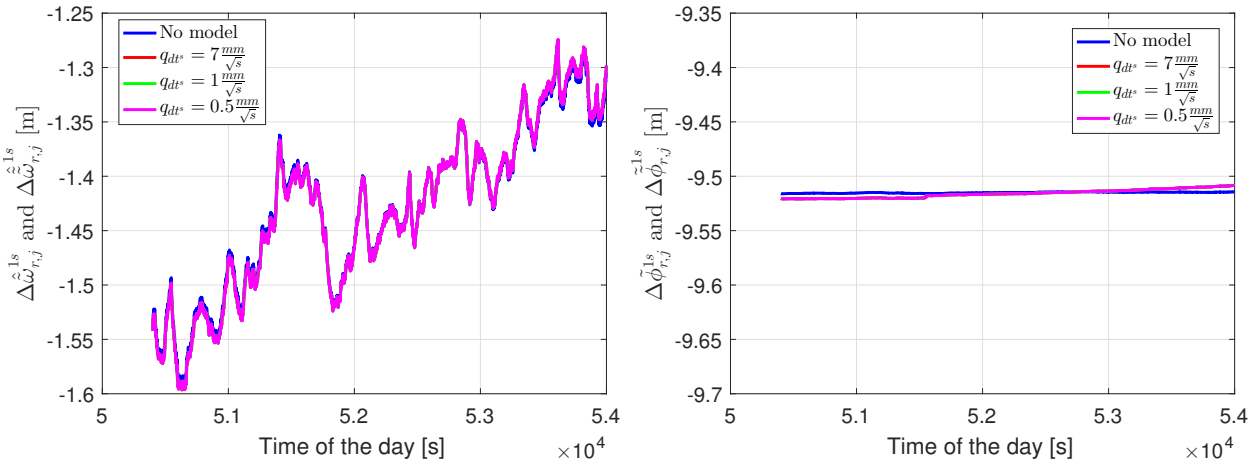

(a) $\Delta\hat{\tilde{\omega}}^{1s}_{r,j}$ and $\Delta\hat{\tilde{\tilde{\omega}}}^{1s}_{r,j}$ (G07 and G09)

(b) $\Delta\tilde{\phi}^{1s}_{r,j}$ and $\Delta\tilde{\tilde{\phi}}^{1s}_{r,j}$ (G07 and G09)

Fig. 6. (a) The residual between-satellite combined network corrections (see Eqs. (26) and (27)) and (b) those after adding the O-C terms of the phase observations (see Eqs. (29) and (30)) of station WBEE for satellites G07 and G09 without and with satellite clock models from 14:00 to 15:00 on March 28, 2017.

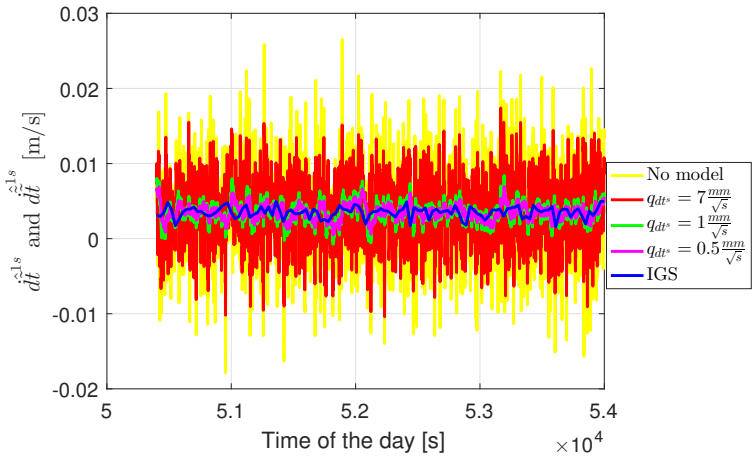

Fig. 7. Estimates of the between-satellite clock rates for satellites G07 and G09 from 14:00 to 15:00 on March 8, 2017. The yellow line represents the estimates of the between-satellite clock rates obtained by fitting polynomials (see Eq. (35)). The blue line represents the estimates of the between-satellite clock rates computed using the IGS final clock products (see Eq. (39)).

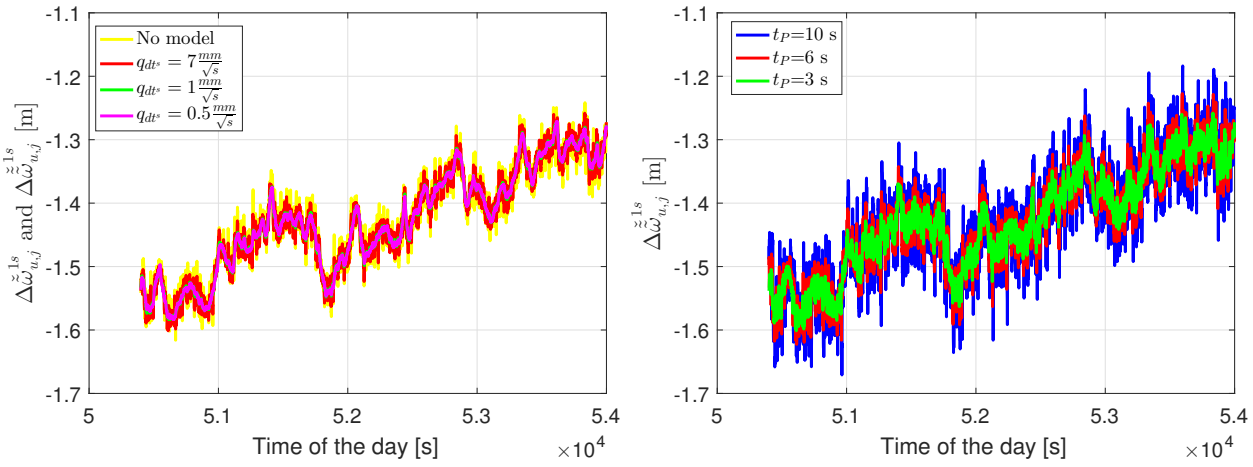

(a) Different satellite clock constraints

(b) Different prediction time

Fig. 8. Residuals of the predicted between-satellite combined network corrections (see Eqs. (40) and (41)) for user station PKVL and the satellites G07 and G09 from 14:00 to 15:00 on March 28, 2017 (a) without and with applying different satellite clock constraints with a prediction time of 3 s and (b) applying a satellite clock model of $q_{dt^s} = 7$ mm/$\sqrt{\text{s}}$ with different prediction time.

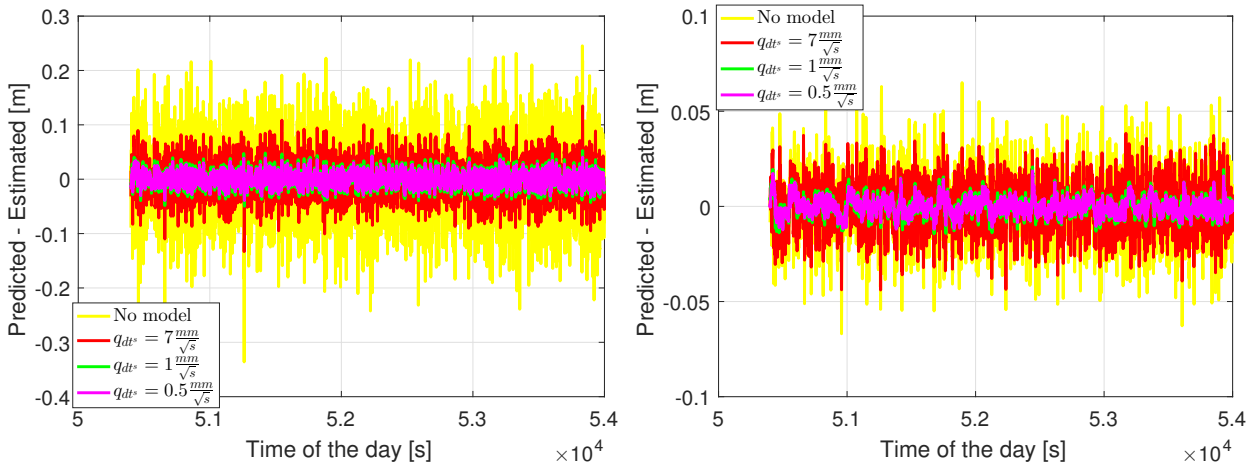

(a) Between-satellite clocks (b) Between-satellite combined corrections

Fig. 9. Differences of (a) the predicted and estimated between-satellite clocks (see Eqs. (33) and (34)) and (b) the predicted and estimated between-satellite combined network corrections (see Eqs. (36) and (37)) for G07 and G09 and user station PKVL from 14:00 to 15:00 on March 28, 2017. The latency in case of prediction is 3 s.

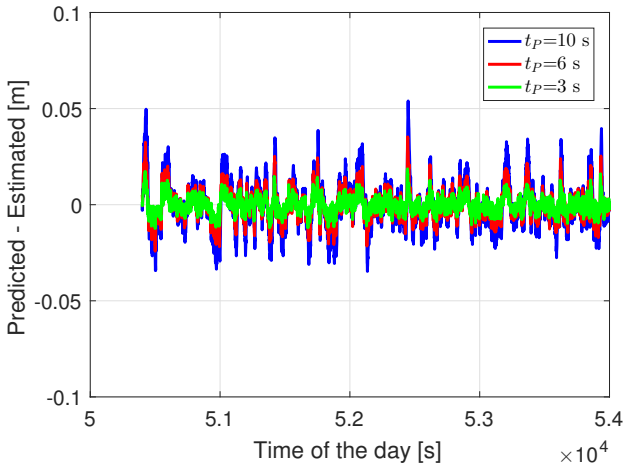

Fig. 10. Differences of the predicted and estimated between-satellite combined network corrections (see Eqs. (36) and (37)) for G07 and G09 and user station PKVL from 14:00 to 15:00 on March 28, 2017 applying satellite clock model with q_{dt^s} of 0.5 mm/$\sqrt{\text{s}}$ and latencies of 3, 6 and 10 s.

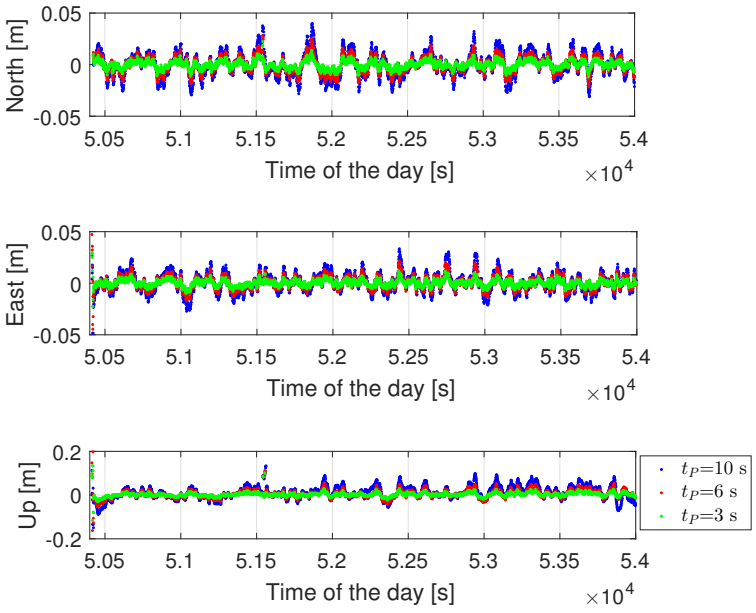

Fig. 11. Coordinate differences for user station PKVL using predicted network corrections (with a q_{dt^s} of 0.5 mm/$\sqrt{\text{s}}$ and a latency of 3, 6 and 10 s) and estimated network corrections in the North-, East- and Up-directions from 14:00 to 15:00 on March 28, 2017. The y-axis is scaled to -5 and 5 cm for the horizontal coordinates, and to -2 and 2 dm for the vertical coordinates. The results are based on partial ambiguity resolution with a pre-defined success rate of 99.99%.

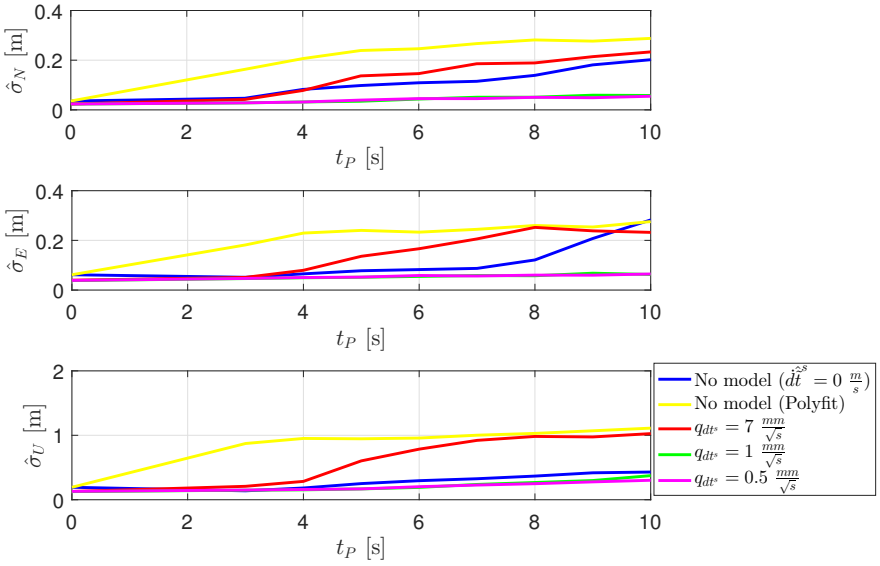

Fig. 12. The overall RMS of the North-, East- and Up-coordinate increments (with respect to the ground truth) using the estimated and the predicted network corrections from 6:00 to 7:00, from 14:00 to 15:00 and from 22:00 to 23:00 (in GPST) on March 28, 2017 with a latency ranging from 3 to 10 s based on partial ambiguity resolution. The yellow and the blue lines represent the cases using the $\dot{\hat{\tilde{dt}}}^s$ obtained by post fitting polynomials (see Eq. (35)) and directly setting the values to 0 m/s, respectively. The red, the green and the magenta lines represent the cases using $\dot{\hat{\tilde{dt}}}^s$ obtained by modelling satellite clocks in the network Kalman filter with q_{dt^s} of 7, 1 and 0.5 mm/$\sqrt{\text{s}}$, respectively.